JOURNAL OF GEOPHYSICAL RESEARCH, VOL. 115, B05102, doi:10.1029/2009JB006820, 2010

Deep water methane hydrates in the Arctic Ocean: Reassessing the significance of a shallow BSR on the Lomonosov Ridge

Matthew O'Regan[1,2] and Kathryn Moran[1,3]

Received 25 July 2009; revised 2 December 2009; accepted 18 December 2009; published 20 May 2010.

[1] Recently published multichannel seismic data from the Lomonosov Ridge image a reversed polarity bottom-simulating reflector (BSR) tentatively attributed to the presence of deepwater marine hydrates and recognized throughout a survey area exceeding 100,000 km^2. In addition to the importance of these findings for estimating Arctic hydrate reserves, if shown to correspond to the base of the hydrate stability zone, this seismic marker could provide a means for expanding spatial cover of heat flow data in deepwater settings of the Amerasian Basin, where little is known about the tectonic origin and nature of plate boundaries. As an initial test on the validity of this assumption, we develop a petrophysical model using sediments collected from circumpolar regions of the Lomonosov Ridge to derive an estimate of surface heat flow patterns from the BSR. The results show that the BSR inferred geothermal gradient and surface heat flow are exceedingly high when compared to published regional measurements. Although potential errors in the analysis may explain some of this discrepancy, the observation that the BSR remains at a constant subbottom depth despite large variations in water depths (>2400 m) and relative sedimentation rates provides additional evidence that it cannot mark the base of the hydrate stability zone. A further understanding of its origin requires a more detailed investigation of the existing seismic data and highlights the need for renewed collection of heat flow data from the Arctic Ocean.

Citation: O'Regan, M., and K. Moran (2010), Deep water methane hydrates in the Arctic Ocean: Reassessing the significance of a shallow BSR on the Lomonosov Ridge, *J. Geophys. Res.*, *115*, B05102, doi:10.1029/2009JB006820.

1. Introduction

[2] Gas hydrates are ice-like substances containing low molecular weight gases (primarily methane). They form naturally in marine sediments under suitable pressure and temperature (P-T) conditions when the pore water saturation of the gas exceeds its solubility [*Trehu et al.*, 2006; *Xu and Ruppel*, 1999]. Methane hydrates are stable in marine sediments at water depths exceeding a few hundred meters and are common on continental margins and slopes worldwide where adequate amounts of organic carbon are available for microbial or thermogenic degradation. In polar regions, hydrates are also found in abundant quantities beneath onshore and offshore permafrost deposits that underlie the broad continental shelves [*Weaver and Stewart*, 1982; *Kvenvolden*, 1993]. Initial volumetric estimates of hydrate bearing sediments in the Arctic rivaled global estimates from the 1970s and 80s and assumed hydrates were present on 75% of the area that lay within an 80 km seaward limit of the 400 m isobath (~525,000 km^2) [*Kvenvolden and Grantz*, 1990]. These estimates explicitly assumed that it was only on the shelves and near major rivers (Mackenzie and Lena) where substantial organic matter was deposited to allow hydrates to accumulate.

[3] The presence of gas hydrates are commonly inferred from seismic reflection data where the base of the hydrate stability zone (BHSZ) can correspond to a reversed polarity reflector that mimics the shape of the seafloor and crosscuts stratigraphic reflectors [*Shipley et al.*, 1979]. The acoustic impedance contrast responsible for the BSR arises from the presence of free gas below the depth at which hydrates are stable [*Holbrook et al.*, 1996]. However, results from Deep Sea Drilling (DSDP) and Ocean Drilling Program (ODP) expeditions have shown that a BSR is not a ubiquitous feature of hydrate bearing sediments, nor laterally continuous in regions where hydrates are present [*Wood and Ruppel*, 2000]. The occurrence and position of the BSR in relation to the hydrate stability field and the zone of gas hydrate occurrence depends on local variations in methane flux, pore water solubility of methane [*Xu and Ruppel*, 1999] and the zone of active sulphate reduction [*Borowski et al.*, 1999].

[4] On a series of multichannel seismic reflection (MCS) profiles collected from the Lomonosov Ridge (LR) in the Arctic Ocean, *Jokat* [2005] reported the occurrence of a reversed polarity BSR potentially related to the presence of marine hydrates. The BSR is a pervasive feature on 900 km

[1]Graduate School of Oceanography, University of Rhode Island, Narragansett, Rhode Island, USA.
[2]Department of Geological Sciences, Stockholm University, Stockholm, Sweden.
[3]Department of Ocean Engineering, University of Rhode Island, Narragansett, Rhode Island, USA.

0148-0227/10/2009JB006820

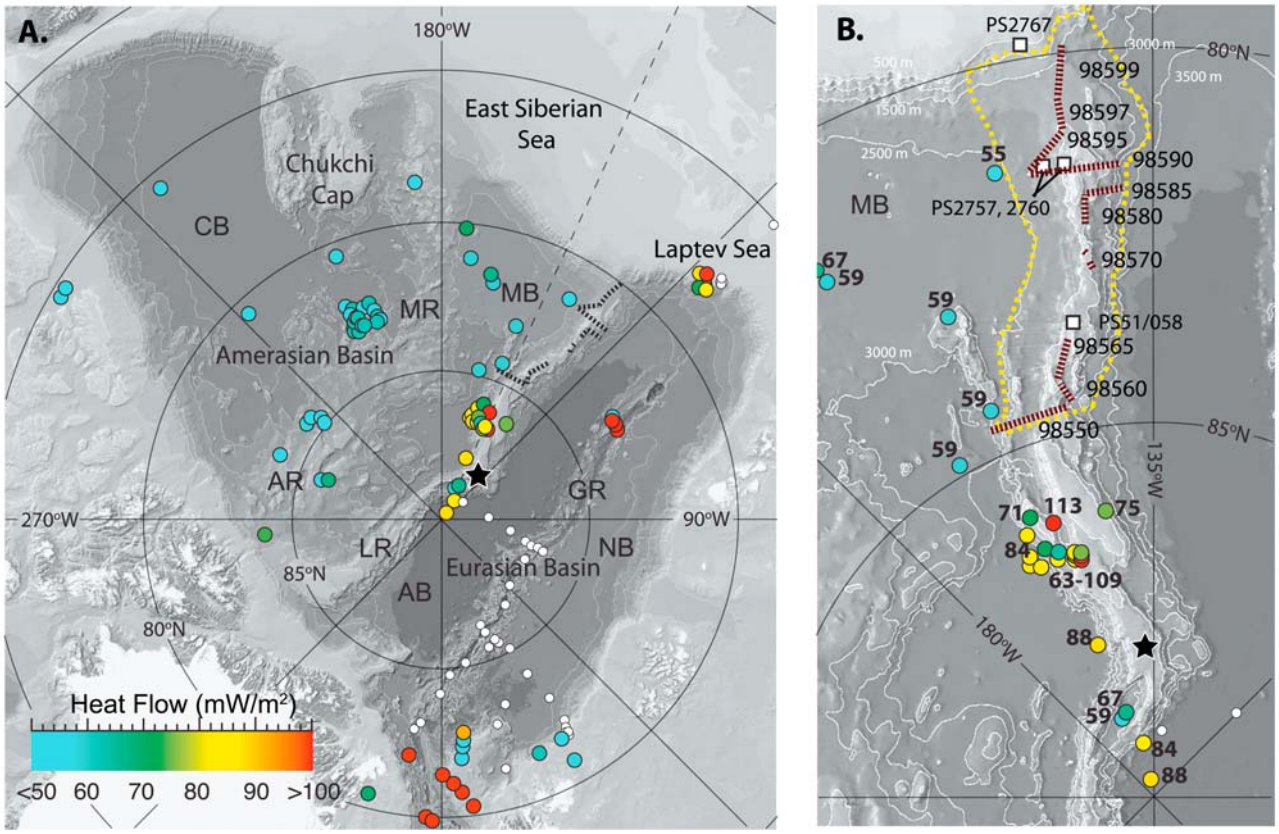

Figure 1. (a) Bathymetric map of the Arctic Ocean [*Jakobsson et al.*, 2008] overlain with color coded heat flow measurements from the world heat flow database (www.heatflow.und.edu) [*Pollack et al.*, 1993] (displayed data compiled in Data Set S1). Location of ACEX sites shown by black star. White circles represent unpublished heat flow data from *Polarstern* cruises in 1987, 1998 and 2001. Seismic lines collected during ARK-XIV-1998 are indicated by hatched lines. (b) Detail of the Lomonosov Ridge showing names of seismic lines and values of published surface heat flow measurements. Dashed yellow line encompasses the seismic survey area and exceeds 100,000 km^2. Location of cores PS51/058, PS2767, PS2760 and PS2757 used to check the validity of the regional compaction curve are shown. AB = Amundsen Basin, AR = Alpha Ridge; CB = Canada Basin; GR = Gakkel Ridge; LR = Lomonosov Ridge; MB = Makarov Basin; MR = Mendeleev Ridge; NB = Nansen Basin.

of seismic data collected between 80 and 84.5°N of the Siberian margin during the ARK-XIV-1998 expedition [*Jokat*, 1999], but is not present on MCS data from circumpolar regions of the LR, despite similar experimental set ups during 1991 and 1996 expeditions [*Futterer*, 1992; *Kristoffersen et al.*, 1997]. The integrated area of the surveyed region exceeds 100,000 km^2, with the BSR extending beyond the survey lines into both the Makarov and Amundsen Basins (Figures 1 and 2). These results provide the first indirect evidence that marine hydrates may exist on the submarine ridges and deep water basins of the Arctic Ocean and are important for considering the potential reservoir size of Arctic hydrates. Furthermore, by possibly marking the P-T phase boundary between gas hydrates and free gas [*Hyndman and Spence*, 1992], if the BSR does correspond to the BHSZ it represents an isotherm that can be used to derive an approximation of surface heat flow [*Yamano et al.*, 1982]. This provides a powerful tool for expanding the spatial coverage and resolution of heat flow data, critical for elucidating the tectonic and geodynamic evolution of the Eurasian and Amerasian Basins.

[5] Here we investigate the likelihood that the BSR imaged on the Lomonosov Ridge corresponds to the BHSZ. We accomplish this by developing a petrophysical model to estimate the pressure at the BSR depth, calculate the inferred geothermal gradient from thermodynamic considerations of hydrate stability using the CSMHyd program [*Sloan*, 1998], develop a regional porosity–thermal conductivity transform to estimate surface heat flow, and compare these with regionally collected in situ heat flow measurements. Our results show that the shallow nature of the BSR on the Lomonosov Ridge (~200 ms two-way traveltime (TWT)) requires regional heat flow of ≈145 mW/m^2 if it marks the BHSZ. This is more than twice the magnitude of previously published data from the region, and cannot be reconciled by considering the uncertainties and potential errors in the calculations. Coupled with the observation that the BSR does not shoal in shallower water depths, it is clear that the BSR cannot be interpreted as marking the BHSZ, and a more extensive analysis of the seismic data with additional constraints on regional geothermal patterns are required to understand its origin.

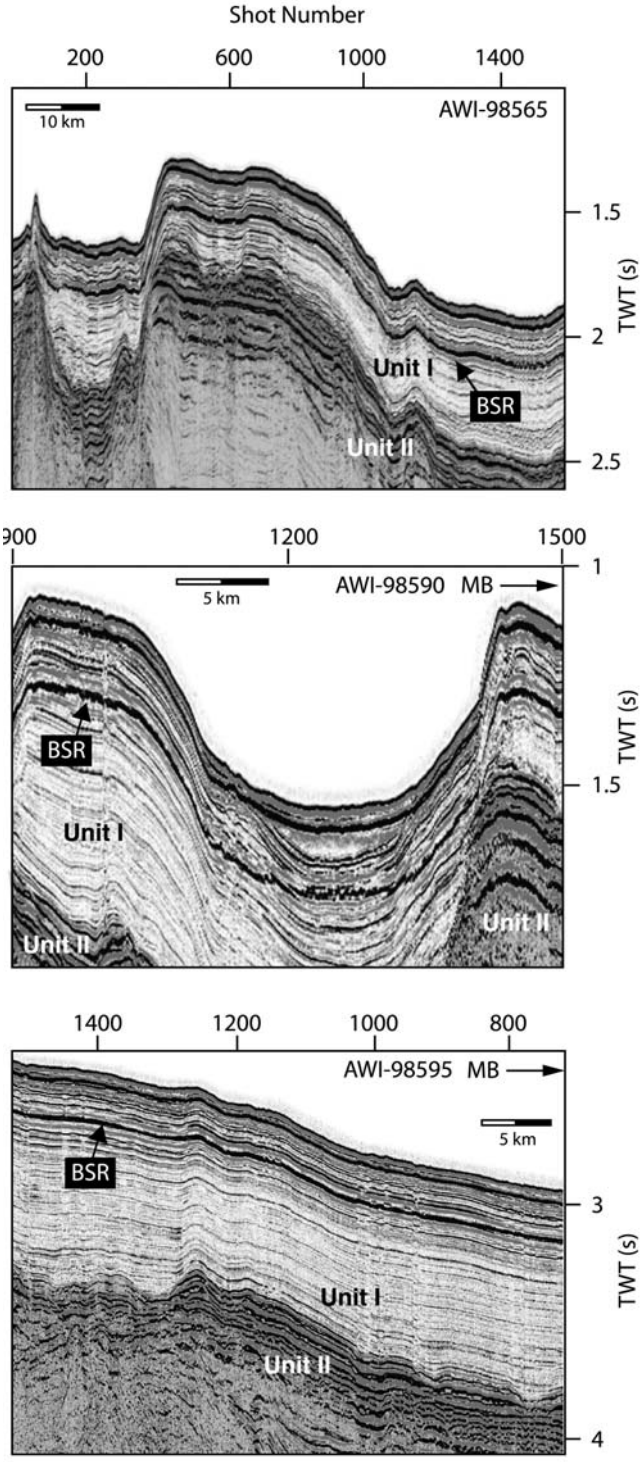

Figure 2. Examples of the reported BSR on seismic lines from the Lomonosov Ridge (adapted from *Jokat* [2005]). Grey shading is used to accentuate the division of Seismic Unit I and II. Location of seismic lines are shown in Figure 1b. MB indicates direction of Makarov Basin on cross-strike profiles.

1.1. Geologic Setting

[6] The Lomonosov Ridge is a 1650 km long segment of continental crust dividing the Arctic Ocean into the Amerasian and Eurasian Basins. It rifted from the Barents-Kara shelf when seafloor spreading extended into the Arctic Ocean along the Gakkel Ridge in the late Paleocene (~56 Ma) [*Vogt et al.*, 1979]. While the Cenozoic opening of the Eurasian Basin is well constrained by marine magnetic lineations [*Vogt et al.*, 1979; *Brozena et al.*, 2003; *Glebovsky et al.*, 2006] aeromagnetic interpretations in the Canada Basin are hampered by a thick sedimentary cover and the likely formation of the Basin during the Long Magnetic Normal period between 125 and 83.5 Ma [*Taylor et al.*, 1981; *Grantz et al.*, 1990]. Thus the age of the Amerasian Basin remains loosely constrained to the late Mesozoic. When coupled with the absence of diagnostic fossil plate boundaries, these ambiguities have prevented the establishment of a definitive tectonic model to describe the opening of the Amerasian Basin [*Grantz et al.*, 1990; *Cochran et al.*, 2006; *Kuzmichev*, 2009].

[7] Subsequently, the composition and age of the Alpha/Mendeleev Ridge and the Makarov Basin bordering the Lomonosov Ridge remain unclear. Seismic reflection and refraction data from the Makarov Basin reveal crustal thicknesses (15–20 km) and velocity structures that are compatible with either thickened oceanic crust or thinned and underplated continental crust [*Sorokin et al.*, 1999; *Lebedeva-Ivanova et al.*, 2006; *Alvey et al.*, 2008] and estimates for the timing of its formation range from the early Cretaceous to the early Eocene [*Taylor et al.*, 1981; *Grantz et al.*, 1990].

[8] In circumpolar regions, the Lomonosov Ridge is a relatively narrow (50–70 km), flat-crested bathymetric high sitting 1000–1500 m below sea level (mbsl) and capped with up to 500 m of Cenozoic sediments. Its overall morphology and structure change toward the Siberian Margin where south of 85.5°N it widens to over 200 km and is composed of a series of blocks and grabens that are presumably an artifact of rifting from the Barents-Kara shelf [*Jokat*, 2005; *Cochran et al.*, 2006]. Bathymetric, seismic and gravity data indicate the Eurasian margin of the Lomonosov Ridge has a structure similar to other orthogonally rifted nonvolcanic continental margins with a set of rotated fault blocks stepping down into the Amundsen Basin where a sharp gravity gradient defines the transition to oceanic crust [*Jokat et al.*, 1992; *Jokat et al.*, 1995; *Cochran et al.*, 2006]. The Amerasian flank of the Lomonosov Ridge is less well defined. Close to the Siberian margin, a negative gravity anomaly paralleling the 155°E meridian is suggested to mark the transition from rifted continental crust to possible oceanic crust [*Jokat*, 2005] (Figure 1). This delineation of the Amerasian flank is supported by *Cochran et al.* [2006] who attribute the widening of the ridge toward the Siberian margin as evidence for the rotational opening of the Amerasian Basin.

[9] During the summer of 2004, the Integrated Ocean Drilling Programs (IODP) Arctic Coring Expedition (ACEX) cored the Cenozoic sequence on the crest of the Lomonosov Ridge at ~88°N [*Backman et al.*, 2006; *Moran et al.*, 2006]. Drilling during ACEX recovered samples from above and below a seismically recognized Cenozoic-Mesozoic unconformity [*Jokat et al.*, 1992; *Jokat et al.*, 1995; *Backman et al.*, 2008] that likely formed when the Lomonosov Ridge was rifted from the Barents-Kara shelf (Figure 3). However,

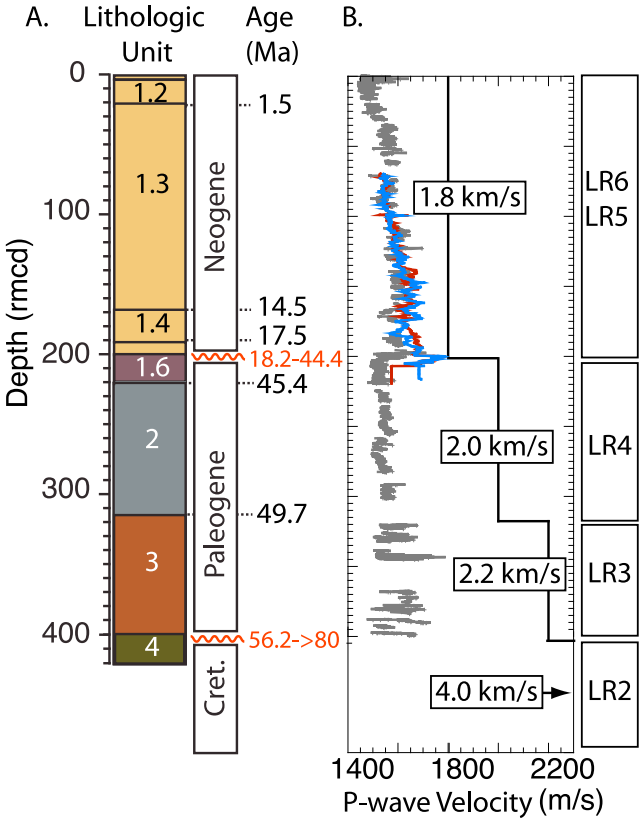

Figure 3. (a) Depth and age of lithologic boundaries in the ACEX record [*Backman et al.*, 2008]. (b) Comparison of compressional wave velocity determined by multisensor core logger (MSCL) measurements on recovered cores (gray line), in situ measurements from downhole wireline logging (red and blue lines) and the sonobouy-modeled velocities. Seismic Units LR2 through 6 defined by *Jokat et al.* [1995] and correlated to the ACEX record by *Jakobsson et al.* [2006].

drilling also uncovered another 26 million year (Myr) hiatus in the Cenozoic sediments on the ridge. This mid-Cenozoic hiatus separates middle Eocene biosiliceous rich sediments (44.4 Ma) from predominantly glaciomarine sediments deposited since the early middle Miocene (18.2 Ma) and occurs at a depth of 198.7 mbsf [*Backman et al.*, 2008] (Figure 3). Drilling results indicate a shallow water setting for the Lomonosov Ridge before and after the hiatus [*Sangiorgi et al.*, 2008], evidence used to argue for either an abnormal postrifting subsidence pattern and/or large-scale sea level variations occurring within a potentially land-locked Arctic Ocean through the mid-Cenozoic [*O'Regan et al.*, 2008]. The shift from biosiliceous to glaciomarine modes of sedimentation (which occurs above the mid-Cenozoic hiatus) is attributed to the opening and widening of the Fram Strait in the middle Miocene, and the subsequent ventilation of intermediate and deep waters [*Jakobsson et al.*, 2007].

[10] The seismic data from south of 85°N, where the flat-crested monolithic segment of the LR ends, can be described using two basic seismic units. A conformably layered unit of low impedance contrasts and an average thickness of < 1 s two-way traveltime (TWT) (hereafter referred to as seismic Unit 1) sits conformably on a set of high-amplitude reflections that define the top of a basin-thickening sequence (seismic Unit II) [*Jokat*, 2005]. The existing interpretation is that the division between these two units represents the boundary between synrift and postrift sediments, implying an age at or around the Cenozoic-Mesozoic boundary [*Jokat*, 2005]. Unlike the circumpolar regions of the ridge, there is no clear erosional surface across this boundary. Concordant with this observation is a more gradual change in the modeled compressional wave velocities, which led to the suggestion that this segment of the Lomonosov Ridge was at initially deeper water depths during rifting from Barents-Kara shelf [*Jokat*, 2005]. Within seismic Unit I there is no indication of either an unconformity or a large-scale shift from biosiliceous to glaciomarine sediments in the interpreted Cenozoic cover, and it remains possible that the current boundary between the two primary seismic units is younger, and is related to either the end of basin-wide biosiliceous and organic rich sedimentation in the middle Miocene or alternatively represents the ongoing conversion of Opal A to C/T [*O'Regan et al.*, 2010]. However, irrespective of the age of this boundary, the BSR identified on these lines occurs at a relatively constant depth of ~200 ms, and falls near the top of the Cenozoic sequence within Miocene or younger sediments (Figure 2). Equivalent sediments from ACEX are described by a single lithologic unit of relatively homogenous, glaciomarine silty clays that is divided into 3 subunits based on changes in sediment color and texture [*Backman et al.*, 2006; *Moran et al.*, 2006].

2. Methods

[11] The BSR on seismic data from the ARK-XIV-1998 cruise is identified on the published lines from *Jokat* [2005]. At each of the marked shotpoints the TWT to the seafloor and BSR were extracted using digitizing software. By initially treating the BSR as being coincident with the BHSZ, we assume that it marks the P/T phase boundary of hydrate stability. We then develop a petrophysical model to determine the pressure at its depth of occurrence, the thermal conductivity of the overlying sediments, and calculate the inferred surface heat flow.

[12] There are three primary petrophysical properties that are required to calculate heat flow from a BSR; the compressional wave velocity, bulk density and thermal conductivity. In this model we use published compaction trends from sediments at ACEX [*O'Regan et al.*, 2010] to develop a porosity-depth function, and use this to calculate the integrated density and thermal conductivity of the overlying sediment column. Each of the steps and assumptions in constructing the model are outlined below.

2.1. Effective Stress–Porosity Transform

[13] Mechanical compaction is the principal mechanism responsible for porosity loss in the upper few hundred meters of marine sediments and is driven by increasing effective stress as sediments accumulate on the seafloor. Intrinsic sediment properties (composition and grain size) determine the rate and magnitude of compaction. In geotechnical engineering it is common to define the void ratio (e) as a logarithmic function of effective stress (σ'):

$$e = e_o - Cc \log(\sigma'), \quad (1)$$

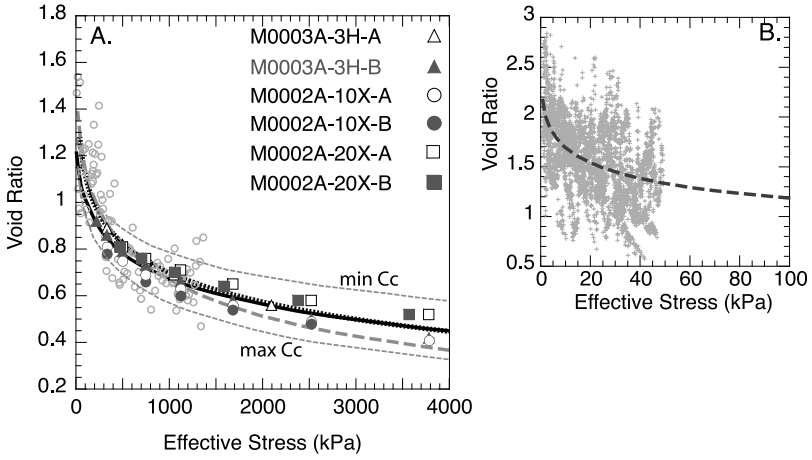

Figure 4. (a) Results from 6 incremental load consolidation tests performed on ACEX samples (large symbols). The average compaction curve is displayed by the thick black line. Rebound corrected index property data from the ACEX borehole are shown for comparison (small gray circles). A logarithmic fit to these data yield a field curve with similar compaction characteristics to the laboratory tests (black dashed line). Thin gray dashed lines indicate the upper and lower bounds for the regional compaction curve, derived by adding/subtracting the standard deviation from the average laboratory derived *Cc* estimate. Thick gray dashed line represents the best fit to rebound-corrected void ratio-effective stress data from 4 cores collected south of 83°N (PS51/058, PS2767, PS2760, PS2757). (b) Compiled data used to define this fit are shown and taken from F. Niessen (Physical properties data of sediment cores from the polar oceans, unpublished data, 2002, available at http://www.wdc-mare.org) and *Stein et al.* [1999] (available from F. Niessen (Physical properties of sediment core PS2757-8, available at http://doi.pangaea.de/10.1594/PANGAEA.50569, 1996; Physical properties of sediment core PS2760-6, available at http://doi.pangaea.de/10.1594/PANGAEA.50599, 1996; Physical properties of sediment core PS2767-4, available at http://doi.pangaea.de/10.1594/PANGAEA.50572, 1996) and R. Stein et al. (Physical properties of sediment core PS51/067-1, http://doi.pangaea.de/10.1594/PANGAEA.205438, 2004).

where e_o is the void ratio when σ' = 1kPa, and *Cc* the *compression index* [*Holtz and Kovacs*, 1981]. The void ratio is related to fractional porosity through:

$$\phi = \frac{e}{(1+e)}. \tag{2}$$

[14] One-dimensional incremental load consolidation tests on 9 samples were performed on material recovered during ACEX [*O'Regan et al.*, 2010]. Six of these samples (of Miocene age and younger), recovered from between 18 and 88 mbsf, display very consistent compaction characteristics (e_o, *Cc*) when reconsolidated to effective stresses up to 10 MPa. Relationships between porosity and effective stress for these samples also show close agreement with rebound corrected porosity profiles from higher-resolution index property sampling down to the base of lithologic subunit 1.3 (at 169 mbsf) (Figure 4).

[15] These findings imply that from a geotechnical perspective, composition and grain size in central Arctic sediments remain relatively constant from the middle Miocene to present. Furthermore, the observation that bulk sediment grain size is composed of > 90% wt fine fraction material [*St. John*, 2008] with clay mineralogy indicating a dominant Eurasian source [*Krylov et al.*, 2008] suggests that closer to the Siberian margin the porosity–effective stress relationships from ACEX should be applicable.

[16] To evaluate the validity of this assumption we used measurements of bulk density and porosity to generate void ratio and effective stress estimates for 4 cores collected from the Lomonosov Ridge/Siberian margin between 83 and 79°N (Figures 1b and 4b). Rebound corrections were made by assuming a recompression index (*Cr*) of 0.1, in keeping with results from ACEX test results [*O'Regan et al.*, 2010]. Only data with a void ratio of < 3 (porosity < 75%) were used to define the combined compaction curve (Figure 4b). While the limited stress range covered by these shallow penetrating cores introduces large uncertainty into the extrapolated best fit line, the overall trend is compatible with the laboratory test and field data from ACEX. However, to adequately account for spatial variations in porosity–effective stress relationships, we adopt the average compaction characteristics from the consolidation tests at ACEX, and use the standard deviation for the coefficient of consolidation (*Cc*) to define an upper and lower bound (Figure 4a) (Table 1).

2.2. Depth–Effective Stress Transform

[17] To convert the effective stress–porosity transform(s) into porosity-depth we draw on basic phase relationships. Effective stress is defined as:

$$\sigma' = \rho' g z, \tag{3}$$

where ρ' is the buoyant density of the sediments (kg/m^3), g is the acceleration due to gravity (m/s^2) and z the depth

Table 1. Summary and Comparison of Consolidation Characteristics (e_o, Cc) Derived From Laboratory and Field Data[a]

Compaction Curve	e_o	Cc
Average laboratory curve	1.804	0.377 ± 0.035
Minimum Cc	1.804	0.342
Maximum Cc	1.804	0.412
ACEX field curve	1.950	0.418
Other cores	2.195	0.510

[a]Details on consolidation sampling and tests results are from *O'Regan et al.* [2010].

below seafloor (m). The buoyant density is found by subtracting the density of seawater (ρ_W = 1024 kg/m^3) from the sediment bulk density (ρ_B). Rewriting equation (3) in terms of porosity gives:

$$z = \frac{\sigma'}{([\rho_G - \phi(\rho_G - \rho_W)] - \rho_W)g}, \quad (4)$$

where ρ_G is the grain density (kg/m^3) and ϕ the fractional porosity. Equation (4) illustrates how the relationship between depth and effective stress depends on the porosity–effective stress relationship and the grain density of the sediments used to convert the porosity estimate into bulk density.

[18] The average grain density of sediments in lithologic subunits 1.1 to 1.3 from ACEX (equivalent to the upper 169 mbsf) (Figure 3) is 2.71 g/cm^3 with a standard deviation of 0.07 [*O'Regan*, 2008]. Combining equations (1), (2) and (4) produces a single expression linking depth and effective stress:

$$z = \frac{\sigma'}{\left[([\rho_G - \left(\frac{(e_o - Cc\log(\sigma'))}{1+(e_o - Cc\log(\sigma'))}\right)(\rho_G - \rho_W)] - \rho_W)*g\right]}, \quad (5)$$

that is solved using the three compaction functions (Figure 4a) and grain densities of 2.64, 2.71 and 2.78 g/cm^3. This allows the derivation of three end-member effective-stress depth relationships. The best approximation (Model 1) uses the average laboratory consolidation curve and a ρ_G of 2.71 g/cm^3. The minimum effective stress at depth (Model 2) is found by using the minimum Cc coupled with a ρ_G of 2.64 g/cm^3 and the maximum effective stress (Model 3) is defined using the maximum Cc and a ρ_G of 2.78 g/cm^3 (Figure 5). Best fit lines for the three cases are used as the effective-stress depth transforms in the petrophysical model (Table 2).

2.3. In Situ Compressional Wave Velocity

[19] An estimate of the average compressional-wave (p wave) velocity is required to convert TWT into depth. Measured p-wave velocities using the MSCL exist for piston and gravity cores from the Lomonosov Ridge and the adjoining basins. These measurements provide limited constraints on how velocity evolves during burial beyond the upper few meters. MSCL measurements on recovered cores from ACEX show similar downhole trends to the in situ wireline-logging measurements between 70 and 170 mbsf. These measurements provide considerably lower estimates (≈1600 m/s) than those acquired from sonobouy modeling (1800 m/s) [*Jokat et al.*, 1995] (Figure 3). Generally, one would expect core measurements to underestimate the in situ velocity because of differences in the porosity and stress conditions. In this instance, it is peculiar that the core and wireline measurements are similar.

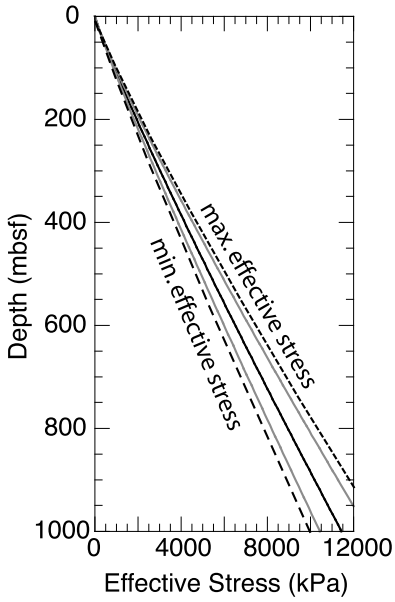

Figure 5. Predicted relationship between depth and effective stress in the upper 1000 mbsf. Heavy black line corresponds to Model (1) in Table 2. Grey lines illustrate the variation introduced by the effective stress–porosity transform used, and the dashed lines the cumulative error of the compaction curve and the assumed grain density. Upper and lower dashed lines correspond to Model (2) and (3) in Table 2.

[20] Core seismic integration suggests that an in situ p wave velocity of 1600 m/s accurately approximates the true velocity based upon the close alignment of reflectors in the synthetic seismogram calculated from core measurements and seismic data collected during ACEX [*Jakobsson et al.*, 2006; *Backman et al.*, 2008] and implies that the sonobouy modeled velocities are too high. This is important, as sonobouy models are the only available constraint on sediment velocity for seismic lines from the ARK-XIV-1998 expedition [*Jokat*, 2005]. The average sonobouy modeled velocity for the sediments containing the BSR varies from line to line (Figure 6). However, they do display similar linear gradients, and when normalized to a seafloor velocity of 1600 m/s result in relatively constant velocity predictions for sediments in the upper 0.4 s TWT.

[21] To account for the disparity in the available measurements we use in situ p wave velocities of 1570, 1670 and 1770 m/s to determine the depth to the BSR. To define a

Table 2. Power Functions Relating Effective Stress to Depth[a]

Model	Comment	A	B
1	Standard model (Cc = 0.377, ρ_G = 2.71)	5.599	1.103
2	Min. Stress (Cc = 0.342, ρ_G = 2.64)	5.451	1.087
3	Max. Stress (Cc = 0.412, ρ_G = 2.78)	5.707	1.122

[a]Depth is σ' = A*z^B where σ' is in kPa and depth (z) in mbsf.

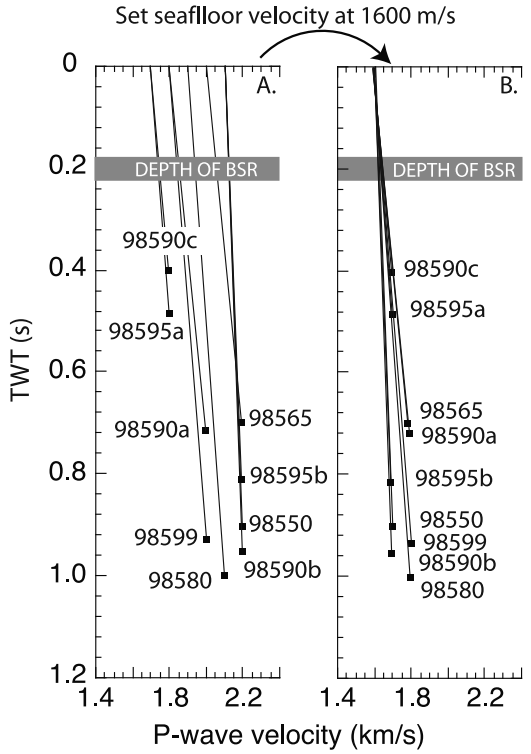

Figure 6. Gradients of sonobouy modeled compressional wave velocity from different stations and seismic lines [*Jokat*, 2005]. See Figure 1b for locations of seismic lines.

conservatively large range of possible in situ pressure and porosity conditions, Model (1) of Table 2 is used in conjunction with a p wave velocity of 1670 m/s, while Model (2) is combined with a velocity of 1770 m/s and Model (3) with 1570 m/s.

[22] At 0.2 s TWT, the three p wave velocities result in depths varying from 157 to 177 mbsf and translate into differences for in situ effective stress estimates of ≈550 kPa (Figure 5). At first glance, this seems to represent a large error for the in situ effective stress estimate, however it is important to point out that it incorporates both the potential error introduced by the depth estimate of the BSR and the depth–effective stress conversions – and given the conservative estimate of these errors it clearly delineates the possible range for the in situ stress estimate. Furthermore, in estimating the temperature at the BSR (section 2.4) it is the total stress that is required. Due to the water depths in which the BSR is found, an average of 80% of the total stress arises from the water column pressure. Total stresses at the BSR range from 10,000 to 30,000 kPa and thereby diminish the impact that the 550 kPa range of effective stresses at the BSR has on the inferred temperature. The differences in the in situ effective stress estimates become more important when defining in situ porosity and thermal conductivity, which are required parameters to calculate the heat flow.

2.4. Temperature at the BSR

[23] For each of the average p wave velocities we calculate the depth to the BSR and the in situ effective stress using one of three effective stress-depth transforms. Empirical and thermodynamic calculations for the P-T stability of methane hydrates require knowledge of the total stress. This involves summing the in situ effective stress estimates with the pressure exerted by the water column:

$$p = \sigma' + \rho_W g z + \rho_W g d, \tag{6}$$

where p is the equivalent hydrostatic pressure (kPa), σ' is derived from the depth–effective stress relationship (kPa) and d is the depth from the sea surface to the seafloor (m). For this calculation, water depth was estimated using the TWT to the seafloor and an average velocity for seawater of 1450 m/s.

[24] Assuming that the BSR represents the BHSZ, we then derive the in situ temperature using the Colorado School of Mines Hydrate stability program (CSMHyd) [*Sloan*, 1998], which allows the user to define in situ gas composition and pressure conditions (p). Above 15 MPa, the CSMHyd predicts lower in situ temperatures for pure seawater-methane systems (NaCl = 3.5 wt%) than empirical equations derived over more limited stress ranges [e.g., *Dickens and Quinby-Hunt*, 1994] (Figure 7). Pore water composition is known to influence the P-T conditions of methane hydrates, with ethane, carbon dioxide, hydrogen sulphide and higher hydrocarbons resulting in an underestimation of the temperature at the BSR, while either higher salinities or nitrogen can result in an

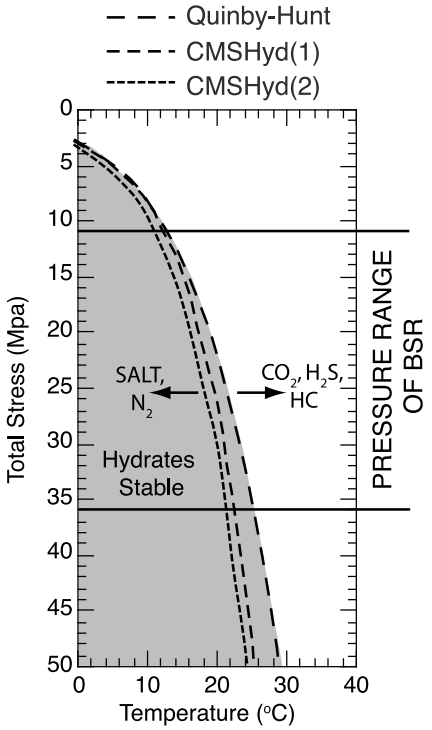

Figure 7. P/T conditions defining the zone of hydrate stability for a seawater (NaCl = 3.5% wt) methane system using the empirical relationship of *Dickens and Quinby-Hunt* [1994] compared to results from the CSMHyd program with (1) a similar seawater-methane system, and (2) using a seawater-methane-nitrogen system with an interstitial gas concentration having 0.9 molar fraction CH_4 and 0.1 molar fraction of N_2.

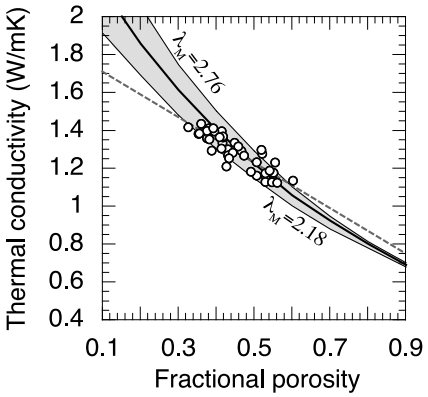

Figure 8. Comparison between the linear fit and geometric mixing model for the porosity–thermal conductivity relationship of ACEX sediments. Circles represent measurements from the upper 165 mbsf of ACEX. The best fit linear relationship (dashed line) is given by: $\lambda = 1.829–1.198\phi$; $R^2 = 0.79$. Results from the geometric mixing model are shown for a matrix conductivity (λ_M) of 2.47 W/mK (middle black line), 2.18 W/mK and 2.76 W/mK.

overestimation [*Grevemeyer and Villinger*, 2001; *Trehu et al.*, 2006] (Figure 7). Calculations made on the P-T conditions of a seawater-methane-nitrogen system with a 0.1 molar fraction of N_2 and 0.9 molar fraction of CH_4 were performed to illustrate the potential difference in the in situ temperatures that can arise (Figure 7).

2.5. Thermal Conductivity and Thermal Resistance Profile

[25] The thermal conductivity of marine sediments is a function of both the conductivity of the matrix material and the pore fluid, and is often expressed using a geometric mixing model:

$$\lambda = \lambda_w^{\phi} \lambda_m^{1-\phi}, \tag{7}$$

where λ is the bulk conductivity in W/mK, λ_w is the conductivity of the pore fluid and λ_m is the conductivity of the matrix [*Grevemeyer and Villinger*, 2001]. Measurements of bulk thermal conductivity were made on thermally equilibrated cores from ACEX using a single needle probe [*Backman et al.*, 2006]. Here we use 37 measurements from ACEX and pair these with the nearest index property derived measurement of sediment porosity. Although a strong linear relationship exists between thermal conductivity and porosity (Figure 8), this can only be assumed to be valid over a limited range of porosities. By rearranging equation (7), assuming a pore water conductivity of 0.60 W/mK [*Grevemeyer and Villinger*, 2001] and solving for λ_m we find that the average matrix conductivity of sediments in the upper 165 mbsf is 2.47 ± 0.29 W/mK. The porosity predicted bulk thermal conductivity (equation 7) compares well with the linear regression results over a limited range of intermediary porosities, but tends to increase (decrease) predictions of λ at lower (higher) porosities (Figure 8). Equation (7) is used with the porosity–effective stress transforms to predict the in situ thermal conductivity.

2.6. Inferred Surface Heat Flow

[26] Heat flow was calculated following the *Bullard* [1939] method, which assumes a linear relationship between the thermal resistance of the sediments (Ω) and temperature (T):

$$T(z) = T_o + q\Omega(z), \tag{8}$$

where T_0 (°C) is the temperature at the seafloor, q (W/m^2) is the heat flow and Ω (m^{2}K/W) is the thermal resistance of the sediments. For all calculations T_0 was set at −0.5°C, consistent with CTD measurements conducted during the ARK-XIV-1998 expedition [*Jokat*, 1999]. The inferred temperature at the BSR was derived in section 2.4. The thermal resistance in equation (8) is the integrated thermal conductivity over a given depth range:

$$\Omega(z) = \int_0^z \frac{dz}{\lambda(z)}, \tag{9}$$

where λ is the average thermal conductivity (W/mK) over the interval dz [*Bullard*, 1939].

2.7. Error Propagation and Summary

[27] To define the widest possible upper and lower bounds for the inferred in situ geothermal gradients and heat flow, we adopt a cumulative error approach. To do this we assume two end –member models in which estimates of the depth to the BSR, in situ porosity and thermal conductivity are combined to either provide the highest or lowest heat flow estimates. Therefore, Model (1), which is the best estimate of the in situ effective stress, is coupled with the average p wave velocity of 1670 m/s and uses an average λ_m of 2.47 W/mK. The resulting λ (bulk thermal conductivity) profile is derived from the porosity prediction using equation (7) (Figure 9). Model (2), which predicts the lowest in situ stress at a given depth (and the highest in situ porosity), is coupled with the highest p wave velocity (1770 m/s) and a λ_m of 2.18 W/mK. This leads to the lowest heat flow estimate. Finally, Model (3) is coupled with the lowest estimate of the in situ p wave velocity (1570 m/s) and the highest λ_m (2.76 W/mK) (Figure 9). This results in the shallowest possible depth to the BSR with the lowest in situ porosity and highest in situ thermal conductivity and yields the highest heat flow estimate. Results from calculations using the three models and the associated p wave velocities are summarized in Data Set S2.[1]

3. Results and Discussion

3.1. Regional Heat Flow Inventory

[28] Direct measurements of heat flow from the Lomonosov Ridge and Makarov Basin are limited to data collected from floating ice stations; including the 1979 LOREX expedition [*Sweeney et al.*, 1982] and the USSR North Pole Drift Station 15 [*Lubimova et al.*, 1973]. Although measurement details and results are lacking, heat flow values between 60–70 mW/m^2 in the Makarov Basin, 60–65 mW/m^2 on the flanks and crest of the Lomonosov Ridge at ~87°N on the Greenland margin side, and 75–85 mW/m^2 in the Amundsen Basin are

[1] Auxiliary materials are available on the FTP site. ftp://ftp.agu.org/apend/jb/2009jb006820/

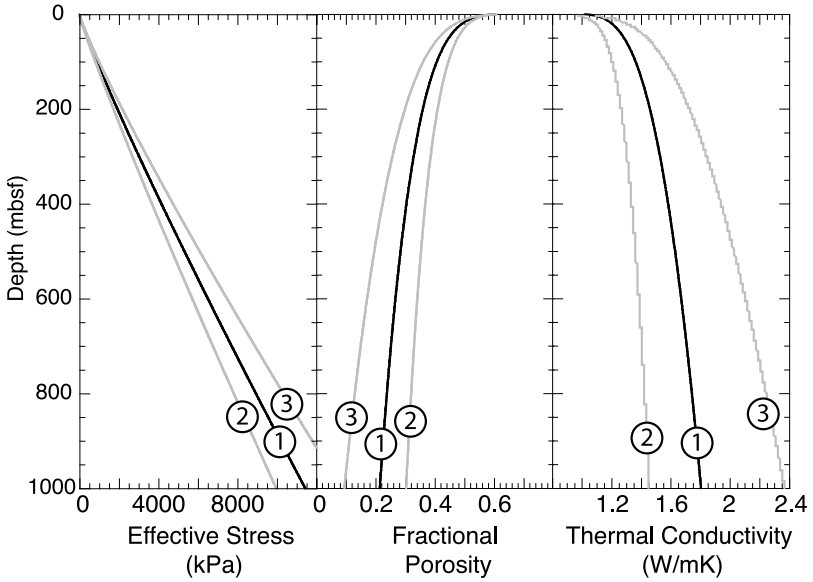

Figure 9. Summary of the petrophysical models used to estimate the pressure at the depth of the BSR and the predicted downhole bulk thermal conductivity profiles used to calculate the surface heat flow. Heat flow calculations are made by integrating the thermal conductivity profile between the seafloor and the depth of the BSR (equation (9)). Numbers refer to the model being used (see Table 2).

reported from the LOREX expedition [*Sweeney et al.*, 1982; *Weber and Sweeney*, 1990]. Additionally, thermal conductivity, temperature gradients and calculated surface heat flow from Russian measurements are stored in the world heat flow databank (Data Set S1) and in the region overlapping with the LOREX measurements record heat flow values of 59–67 mW/m^2 from the intra basin on the Lomonosov Ridge and 84–88 mW/m^2 in the Amundsen Basin (Figure 1b).

[29] An additional 13 Russian measurements are published from the flanks and crest of the Lomonosov Ridge between 85.8 and 86.6 °N and 158.5 and 144.6 °W (Figure 1b). These measurements illustrate a more variable heat flow pattern with values ranging between 59 and 109 mW/m^2. Further toward the Siberian Margin, a few measurements exist from the Makarov Basin, Lomonosov Ridge and Arlis Rise. They all reveal relatively consistent surface heat flow values of 55–65 mW/m^2. The closest measurement to the MCS data has a value of 55 mW/m^2, is located ≈ 40 km from the termination of seismic lines AWI-98595 and AWI-98590 and lies at a longitude of 149.28 °W, implying that it remains on the stretched continental crust of the Lomonosov Ridge (Figure 1).

3.2. Comparison With BSR Derived Heat Flow

[30] Surface heat flow estimates were made at 71 shotpoints on the published seismic data from ARK-XIV-1998. Water depths in which the BSR was identified ranged from 800 to 3250 mbsl, with an average depth of 1560 mbsl. This translates into an average pressure estimate at the seafloor of 15.7 MPa and a range of 8 – 33 MPa (Data Set S2). The average depth and pressure of the water column alone implies that the average temperature at the inferred BHSZ is > 16°C (Figure 7). Due to the influence of the overlying water column, the different petrophysical models produced very little (<1°C) variation in the estimated temperature at the BSR. Averages for Models (1) through (3) were 17.8, 17.6 and 17.4°C, respectively. Using the best approximation provided by Model (1) (Table 2), the average surface heat flow is 146.1 mW/m^2 with a standard deviation of 18.4 mW/m^2. Models (2) and (3) produce averages of 124 ± 14 mW/m^2 and 173.5 ± 22 mW/m^2, respectively. These are 2–3 times higher than regional measurements would suggest and approach values obtained from measurements on the Laptev shelf in an active extensional tectonic setting [*Drachev et al.*, 2003] or on the flanks of the Gakkel Ridge near 83°N [*Lubimova et al.*, 1969] (Figure 1a).

[31] The inferred geothermal gradients, which are more sensitive to errors in p wave velocity used to calculate the depth to the BSR, are similarly high with an average of 105.8 ± 14°C/km for Model (1), 100.8 ± 13°C/km for Model (2) and 111.4 ± 15°C/km for Model (3). This is substantially higher than the closest direct measurement to line AWI-98595, with a reported geothermal gradient of 60°C/km. Although direct measurements tentatively indicate higher geothermal gradients north of 85°N on the Lomonosov Ridge, these also have a lower average (77 ± 31°C/km) (Data Set S1) than those inferred from the BSR derived estimates.

[32] A simplified way of visualizing the data is to plot the average heat flow from each seismic line along a latitudinal gradient from the North Pole to the Siberian margin, and overlay the published measurements that fall on/near the Lomonosov Ridge (Figure 10). While published data may indicate elevated heat flow values as one moves south from 89 to 86°N [*Lubimova*, 1969], the trend does not continue in the off axis measurements between 81.5 and 84.5°N, where the measured heat flow values remain at 50–65 mW/m^2 in contrast to the BSR derived heat flow which increases to ≈145 mW/m^2. An important observation is that the broad range of values derived from the petrophysical models are not sufficient to reconcile the BSR derived heat flow esti-

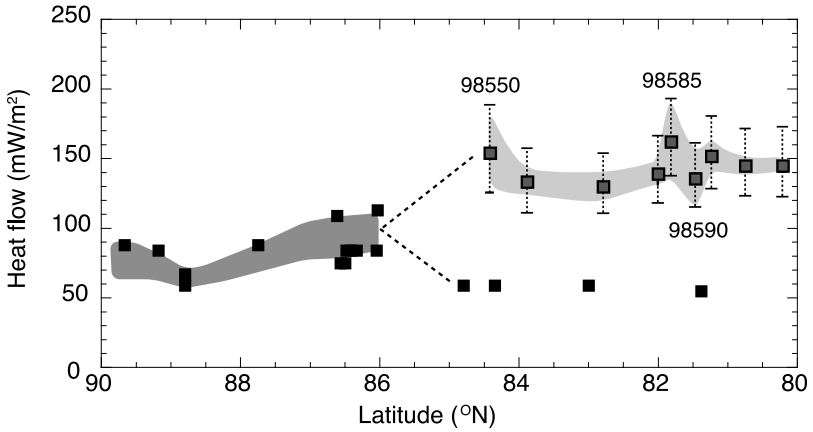

Figure 10. Latitudinal summary of heat flow measurements and BSR derived estimates along the Lomonosov Ridge. Black squares are archived measurements from the world heat flow databank, with dark gray shading accentuating the range of values. Grey squares represent the average heat flow calculated using Model (1) with the standard deviation along each line represented by the light gray shading. Averages from Model (2) and Model (3) are shown by the error bars.

mates and the published measurements from the region, and that the high inferred surface heat flow arises because of the shallow nature of the BSR in relatively deep waters.

3.3. Observations on the Depth to the BSR

[33] The largest variability in the BSR derived heat flow occurs on the cross-strike seismic lines (AWI-98550, 98585, 98590; Figure 1b) where differences in water depth are the greatest. This results in a nearly linear relationship between the depth to the seafloor and the geothermal gradient inferred from assuming that the BSR corresponds to the BHSZ (Figure 11). If the BSR does mark the BHSZ, it should shoal (deepen) in shallower (deeper) water depths as a consequence of changes in pressure and the inferred geothermal gradient would remain relatively constant. Furthermore, the variation that does arise is opposite to what is expected by P-T considerations. For example, on AWI-98595 (Figures 1 and 2), the water depth increases toward the Makarov Basin from 1457 to 2262 m between shotpoints 200 and 1800 but the BSR shoals by ~17 m (Model 1, Data Set S2). Similarly on AWI-98590, the water depth increases from 819 to 2129 m between shotpoints 1500 and 2700, with a corresponding shoaling of the BSR by ~9–12 m. A downslope increase in sedimentation rate cannot explain the observed patterns as this would reduce the surface heat flow and deepen the BSR [*Jessop*, 1990], similar to the expected response to changes in pressure.

[34] A mechanism that could reconcile these observations would be the focusing of heat flow by local topographic variations [*Ganguly et al.*, 2000; *He et al.*, 2007]. *Lachenbruch* [1968] showed that inflections in the slope of the seafloor serve to elevate or reduce local heat flow, with reduced heat

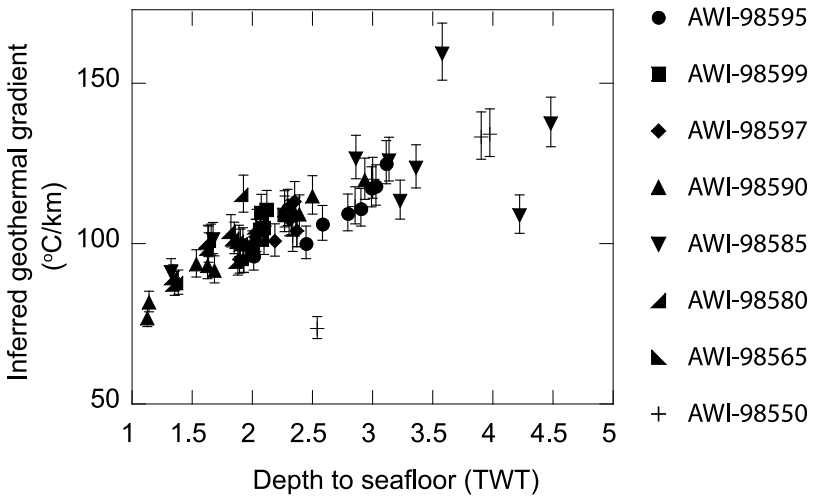

Figure 11. Relationship between the water depth (displayed as the TWT to the seafloor) and the inferred geothermal gradient derived from assuming that the BSR corresponds to the BHSZ. Each point represents the derived geothermal gradient using Model (1) with vertical bars indicating range of values between Models (2) and (3).

flow occurring in regions with a concave downward geometry (i.e., on ridges). Therefore, topographic variations could cause a deepening of the BSR on shallower portions of the ridge despite the lower P-T estimates for the BHSZ. The magnitude of the predicted heat flow anomaly is determined by the angle of the slope. Approximate slope angles on AWI-98585 and AWI-98590 are between 0.5° and 1.5°, respectively, and based on the look-up tables provided by *Lachenbruch* [1968] would result in heat flow variations of less than 5–10%. At the shallow end of AWI-98585 (shot 1800, Data Set S2), this would correspond to a predicted deepening of the BSR by 10–20 m. For comparison, the 805 m change in water depth between shots 200 and 1800 along this same line equate to a 3°C difference in the predicted temperature at the BSR (Model 1, Data Set S2), which translates into a 20–40 m deepening of the BSR depending on whether a geothermal gradient of 125 or 75°C/km is assumed, respectively.

[35] These results highlight two fundamental problems with interpreting the BSR in the classical sense as being coincident with the BHSZ; (1) the BSR derived heat flow is substantially higher than the reported regional measurements, (2) the BSR depth does not change in response to variations in pressure (water depth).

3.4. Can the BSR be Related to Methane Hydrates?

[36] BSR derived estimates of surface heat flow have been made in many geographic and geologic settings [*Yamano et al.*, 1982; *Langseth et al.*, 1990; *Kaul et al.*, 2000; *Grevemeyer et al.*, 2003; *Vanneste et al.*, 2005]. In most instances, there is direct evidence from borehole sampling/logging to link the BSR to the BHSZ and to the base of the gas hydrate occurrence zone (GHOZ). Given these constraints, the method is generally robust. For example, BSR derived estimates at two sites cored on the Blake Ridge during ODP Leg 164 resulted in closer approximations to in situ temperature measurements than extrapolation from shallow penetrating surface measurements [*Wood and Ruppel*, 2000]. For the Lomonosov Ridge, ground-truthing required to assume that the BSR occurs at the BHSZ is lacking, and instead we have shown that for this to be true, regional heat flow must be extremely high, an observation not in keeping with the available measurements.

[37] Beyond recognized uncertainty in the petrophysical model, elevated estimates of the surface heat flow can arise from variations in pore water composition, which can reduce the P-T stability field for hydrates [*Grevemeyer and Villinger*, 2001]. The influence of changing gas composition within the pore spaces was addressed by investigating the impact of nitrogen on the predicted P-T stability field. This was accomplished using the CSMHyd program by employing a hypothetical gas composition with a 0.9 molar fraction of CH_4 and 0.1 molar fraction of N_2. The resulting average heat flow derived from Model (2) (i.e., predicting the lowest heat flow of the petrophysical models) was only reduced from 124.4 to 114.7 mW/m^2 (Data Set S2). Other impurities in the gas composition were omitted as they all serve to raise the stability temperature for hydrates (Figure 7) and would increase the derived heat flow. This basic modeling suggests that absolute magnitudes of the derived heat flow cannot realistically be accounted for by changing the interstitial gas composition. Other mechanisms, including capillary forces in fine-grained sediments, can also inhibit hydrate formation and result in higher estimates of the in situ temperature when compared to estimates based on P-T considerations [*Ruppel*, 1997; *Melnikov and Nesterov*, 1996]. While incorporation of these effects may reduce the existing discrepancy between the magnitude of the calculated heat flow and that derived from regional measurements, these arguments cannot account for the observation that the BSR does not respond to changes in pressure.

[38] Hydrates are dynamic systems that respond to complex biogeochemical and fluid flow patterns [*Trehu et al.*, 2006]. For example, analytical modeling has shown that for the base of the GHOZ to correspond to the BHSZ, a critical flux of methane is required [*Xu and Ruppel*, 1999]. Similarly, while in most deep water settings P-T models predict that hydrates are stable at the seafloor, the upper limit of their distribution is primarily controlled by methane solubility in the pore fluids and bottom waters [*Xu and Ruppel*, 1999]. Their distribution is also limited to depths below the zone of active anaerobic oxidation of methane and sulphate reduction [*Borowski et al.*, 1999]. These constraints on the distribution of hydrates result in the top of the GHOZ being located 10s to 100s of meters below the seafloor [*Trehu et al.*, 2006], and is a potential cause for the growing recognition of a 'double' BSR in some hydrate bearing regions [*Posewang and Mienert*, 1999; *Nouze and Baltzer*, 2003]. Is it then possible that the observed BSR marks the top or base of the GHOZ?

[39] Once again, it is the constant depth of the BSR that is difficult to explain by invoking either of these mechanisms to explain its shallow nature. For the BSR to mark the base of the GHOZ one would need systematic changes in the methane flux to occur in unison with changes in water depth over a very large area. Similarly, it is difficult to argue that the bottom water concentration of methane remains constant over this area, and results in consistent subbottom profiles of methane solubility or the position of the sulphate-methane interface, especially given the recognized differences in relative sedimentation rate between and within the different seismic profiles [*Jokat*, 2005]. Finally, in reported instances where a shallow BSR marks the top of the GHOZ, the polarity of the reflector is normal. This arises through the transition from low velocity free gas intervals within the sediments, to frozen methane hydrate within the GHOZ [*Posewang and Mienert*, 1999]. On published seismic data from the Lomonosov Ridge, the shallow BSR has a reversed polarity with respect to the seafloor, and is clearly not consistent with observations from double BSR bearing hydrate fields in other regions.

4. Conclusions

[40] The shallow BSR imaged on the MCS data from the Lomonosov Ridge shares many characteristics commonly used to infer the presence of marine hydrates, including discordance with stratigraphic reflectors and reversed polarity. By developing a petrophysical model to calculate the pressure at its depth of occurrence, and the thermal conductivity of overlying sediments, we have shown that the inferred surface heat flow is remarkably high if the BSR marks the

base of the hydrate stability zone. Even when conservative (i.e., large) error estimates are incorporated into the modeling, the inferred heat flow remains significantly higher than nearby shallow penetrating measurements. Perhaps more importantly is the observation that the BSR does not shoal in shallower water depths, even though it is found in water depths spanning 2400 m. Together these arguments indicate that the imaged BSR cannot be interpreted in the classical sense as marking the P-T phase boundary between hydrate and free gas. Furthermore, it is difficult to envision a reason why it should be found at such a constant depth across such a large geographic area if it marks a geochemical front within hydrate bearing sediments. Without a more detailed assessment of the seismic data and additional direct measurements of regional heat flow patterns to constrain thermal models, the true nature of the identified BSR remains unknown and its association with an extensive deepwater methane hydrate field remains unproven.

[41] **Acknowledgments.** Financial support was provided by NSF (ODP) grant 0623220. This research was conducted with samples and data from the Integrated Ocean Drilling Program (IODP), an international marine research program dedicated to advancing scientific understanding of the Earth, the deep biosphere, climate change, and Earth processes by sampling and monitoring subseafloor environments.

References

Alvey, A., C. Gaina, N. J. Kusznir, and T. H. Torsvik (2008), Integrated crustal thickness mapping and plate reconstructions for the high Arctic, *Earth Planet. Sci. Lett.*, *274*, 310–321, doi:10.1016/j.epsl.2008.07.036.

Backman, J., et al. (2008), Age model and core–seismic integration for the Cenozoic Arctic Coring Expedition sediments from the LR, *Paleoceanography*, *23*, PA1S03, doi:10.1029/2007PA001476.

Backman, J., K. Moran, D. B. McInroy, and L. A. Mayer (2006), *Arctic Coring Expedition (ACEX)*, *Proc. Integr. Ocean Drill. Program*, *302*, doi:10.2204/iodp.proc.302.2006.

Borowski, W. S., C. K. Paull, and W. Ussler (1999), Global and local variations of interstitial sulfate gradients in deep-water, continental margin sediments: Sensitivity to underlying methane and gas hydrates, *Mar. Geol.*, *159*, 131–154, doi:10.1016/S0025-3227(99)00004-3.

Brozena, J. M., V. A. Childers, L. Lawver, L. M. Gahagan, R. Forsberg, J. I. Faleide, and O. Eldholm (2003), New aerogeophysical study of the Eurasia Basin and Lomonosov Ridge: Implications for Basin development, *Geology*, *31*, 825–828, doi:10.1130/G19528.1.

Bullard, E. C. (1939), Heat Flow in South Africa, *Proc. R. Soc. London, Ser. A*, *173*, 474–502, doi:10.1098/rspa.1939.0159.

Cochran, J. R., M. H. Edwards, and B. J. Coakley (2006), Morphology and structure of the Lomonosov Ridge, Arctic Ocean, *Geochem. Geophys. Geosyst.*, *7*(5), Q05019, doi:10.1029/2005GC001114.

Dickens, G. R., and M. S. Quinby-Hunt (1994), Methane hydrate stability in seawater, *Geophys. Res. Lett.*, *21*, 2115–2118, doi:10.1029/94GL01858.

Drachev, S. S., N. Kaul, and V. N. Beliaev (2003), Eurasia spreading basin to Laptev Shelf transition: Structural pattern and heat flow, *Geophys. J. Int.*, *152*(3), 688–698, doi:10.1046/j.1365-246X.2003.01882.x.

Futterer, D. (Ed.) (1992), ARCTIC'91: The expedition ARK VIII/3 of Rv Polarstern in 1991, *Ber. Polarforsch.*, *107*, 1–267.

Ganguly, N., G. D. Spence, N. R. Chapman, and R. D. Hyndman (2000), Heat flow variations from bottom simulating reflectors on the Cascadia margin, *Mar. Geol.*, *164*, 53–68, doi:10.1016/S0025-3227(99)00126-7.

Glebovsky, V. Y., V. D. Kaminsky, A. N. Minakov, S. A. Merkur'ev, V. A. Childers, and J. M. Brozena (2006), Formation of the Eurasia Basin in the Arctic Ocean as inferred from geohistorical analysis of the anomalous magnetic field, *Geotectonics, Engl. Transl.*, *40*(4), 263–281, doi:10.1134/S0016852106040029.

Grantz, A., S. D. May, P. T. Taylor, and L. A. Lawver (1990), Canada Basin, in *The Arctic Region*, edited by A. Grantz, G. L. Johnson, and W. J. Sweeney, pp. 379–402, Geol. Soc. Am., Boulder.

Grevemeyer, I., and H. Villinger (2001), Gas hydrate stability and the assessment of heat flow through continental margins, *Geophys. J. Int.*, *145*, 647–660, doi:10.1046/j.0956-540x.2001.01404.x.

Grevemeyer, I., et al. (2003), Heat flow over the descending Nazca plate in central Chile, 32°S to 41°S: Observations from ODP Leg 202 and the occurrence of natural gas hydrates, *Earth Planet. Sci. Lett.*, *213*(3–4), 285–298, doi:10.1016/S0012-821X(03)00303-0.

He, T., G. D. Spence, M. Riedel, R. D. Hyndman, and N. R. Chapman (2007), Fluid flow and origin of carbonate mound offshore Vancouver Island: Seismic and heat flow constraints, *Mar. Geol.*, *239*, 83–89, doi:10.1016/j.margeo.2007.01.002.

Holbrook, W. S., et al. (1996), Methane hydrate and free gas on the Blake Ridge from vertical seismic profiling, *Science*, *273*, 1840–1843, doi:10.1126/science.273.5283.1840.

Holtz, R. D., and W. D. Kovacs (1981), *An Introduction to Geotechnical Engineering*, Prentice-Hall, Englewood Cliffs, N. J.

Hyndman, R. D., and G. D. Spence (1992), A seismic study of methane hydrate marine bottom simulating reflectors, *J. Geophys. Res.*, *97*, 6683–6698, doi:10.1029/92JB00234.

Jakobsson, M., et al. (2006), Expedition 302 geophysics: Integrating past data with new results in *Arctic Coring Expedition (ACEX)*, *Proc. Integr. Ocean Drill. Program*, *302*, 1–21, doi:10.2204/iodp.proc.302.102.2006.

Jakobsson, M., et al. (2007), The early Miocene onset of a ventilated circulation regimen in the Arctic Ocean, *Nature*, *447*, 986–990, doi:10.1038/nature05924.

Jakobsson, M., R. Macnab, L. Mayer, R. Anderson, M. Edwards, J. Hatzky, H. W. Schenke, and P. Johnson (2008), An improved bathymetric portrayal of the Arctic Ocean: Implications for ocean modeling and geological, geophysical and oceanographic analyses, *Geophys. Res. Lett.*, *35*, L07602, doi:10.1029/2008GL033520.

Jessop, A. M. (1990), *Thermal Geophysics*, 306 pp., Elsevier, Amsterdam.

Jokat, W. (1999), *Arctic'98: The Expedition ARK-XIVI 1a of Rv Polarstern in 1998*, *Ber. Polarforsch.*, 308, 159 pp.

Jokat, W. (2005), The sedimentary structure of the LR between 88°N and 80°N, *Geophys. J. Int.*, *163*, 698–726, doi:10.1111/j.1365-246X.2005.02786.x.

Jokat, W., Y. Kristoffersen, and T. M. Rasmussen (1992), LR–A double sided continental margin, *Geology*, *20*, 887–890, doi:10.1130/0091-7613(1992)020<0887:LRADSC>2.3.CO;2.

Jokat, W., E. Weigelt, Y. Kristoffersen, T. M. Rasmussen, and T. Schöne (1995), New insights into the evolution of the LR and the Eurasian Basin, *Geophys. J. Int.*, *122*, 378–392.

Kaul, N., A. Rosenberger, and H. Villinger (2000), Comparison of measured and BSR-derived heat flow values, Makran accretionary prism, Pakistan, *Mar. Geol.*, *164*, 37–51, doi:10.1016/S0025-3227(99)00125-5.

Kristoffersen, Y., V. Buravtsev, W. Jokat, and V. Poselov (1997), Seismic reflection surveys during Arctic Ocean-96, Cruise report, in *Polarforskningssekretaariatets arsbok 1995/96*, edited by E. Grönlund, pp. 75–77, Polarforskningssekretariatet, Stockholm.

Krylov, A. A., I. A. Andreeva, C. Vogt, J. Backman, V. V. Krupskaya, G. E. Grikurov, K. Moran, and H. Shoji (2008), A shift in heavy and clay mineral provenance indicates a middle Miocene onset of a perennial sea ice cover in the Arctic Ocean, *Paleoceanography*, *23*, PA1S06, doi:10.1029/2007PA001497.

Kuzmichev, A. (2009), Where does the South Anyui suture go in the New Siberian islands and Laptev Sea?: Implications for the Amerasia Basin origin, *Tectonophysics*, *463*, 86–108, doi:10.1016/j.tecto.2008.09.017.

Kvenvolden, K. A. (1993), A primer on gas hydrates, in *The Future of Energy Gases*, edited by D. G. Howel, *U.S. Geol. Surv. Prof. Pap.*, *1570*, 279– 291.

Kvenvolden, K. A., and A. Grantz (1990), Gas hydrates of the Arctic Ocean region, in *The Arctic Ocean Region. The Geology of North America*, edited by A. Grantz, L. Johnson, and J. F. Sweeney, pp. 539–549, Geol. Soc. Am., Boulder, Colo.

Lachenbruch, A. (1968), Rapid estimation of the topographic disturbance to superficial thermal gradients, *Rev. Geophys.*, *6*(3), 365–400, doi:10.1029/RG006i003p00365.

Langseth, M. G., A. H. Lachenbruch, and B. V. Marshall (1990), Geothermal Observations in the Arctic Region, in *The Geology of North America,* vol. L, *The Arctic Ocean Region*, edited by A. Grantz, G. L. Johnson, and J. F. Sweeney, pp. 133–151, Geol. Soc. Am., Boulder, Colo.

Lebedeva-Ivanova, N. N., Y. Y. Zamansky, A. E. Langinen, and M. Y. Sorokin (2006), Seismic profiling across the Mendeleev Ridge at 82 N: Evidence of continental crust, *Geophys. J. Int.*, *165*, 527–544, doi:10.1111/j.1365-246X.2006.02859.x.

Lubimova, E. A. (1969), Terrestrial heat flow for the USSR and its connection with other Geophenomena, *Bull. Volcanol.*, *33*(1), 341–367, doi:10.1007/BF02596728.

Lubimova, E. A., G. A. Tomara, R. M. Demenitskaya, and A. M. Karasik (1969), Measurement of heat flow across the Arctic Ocean floor in the vicinity of the median hackel ridge, *Dokl. Akad. Nauk SSSR*, *186*, 1318–1321.

Lubimova, E. A., B. G. Polyak, Y. B. Smirnov, R. I. Kutas, F. V. Firsov, S. I. Sergienko, and L. N. Luisova (1973), *Heat flow on the USSR Territory: catalogue of data*, Geophys. Comm. Acad. Sci. USSR, Moscow.

Melnikov, V., and A. Nesterov (1996), Modelling of gas hydrates formation in porous media, in *Proceedings of the Second International Conference on Natural Gas Hydrates*, edited by J. P. Monfort, pp. 541–548, Tapir Acad., Trondheim, Norway.

Moran, K., et al. (2006), The Cenozoic palaeoenvironment of the Arctic Ocean, *Nature*, *441*, 601–605, doi:10.1038/nature04800.

Nouze, H., and A. Baltzer (2003), Shallow bottom-simulating reflectors on the Angola margin, in relation with gas and gas hydrate in the sediments, in *Subsurface Sediment Mobilization*, edited by P. Van Rensbergen et al., *Geol. Soc. Spec. Publ.*, *216*, 191–206.

O'Regan, M. (2008), Data report: High-resolution bulk density, dry density, and porosity records from the Arctic Coring Expedition, IODP Expedition 302, in *Arctic Coring Expedition (ACEX)*, *Proc. Integr. Ocean Drill. Program*, *302*, doi:10.2204/iodp.proc.302.201.2008.

O'Regan, M., et al. (2008), Mid-Cenozoic tectonic and paleoenvironmental setting of the central Arctic Ocean, *Paleoceanography*, *23*, PA1S20, doi:10.1029/2007PA001559.

O'Regan, M., K. Moran, C. P. Baxter, J. Cartwright, C. Vogt, and M. Koelling (2010), Towards ground truthing exploration in the central Arctic Ocean: A Cenozoic compaction history from the Lomonosov Ridge, *Basin Res.*, *22*, 215–235, doi:10.1111/j.1365-2117.2009.00403.x.

Pollack, H. N., S. J. Hurter, and J. R. Johnson (1993), Heat flow from the Earth's interior: Analysis of the global data set, *Rev. Geophys.*, *31*, 267–280, doi:10.1029/93RG01249.

Posewang, J., and J. Mienert (1999), The enigma of double BSRs: Indicators for changes in the hydrate stability field, *Geo Mar. Lett.*, *19*, 157–163, doi:10.1007/s003670050103.

Ruppel, C. (1997), Anomalously cold temperatures observed at the base of gas hydrate stability zone on the US passive continental margin, *Geology*, *25*(8), 699–704, doi:10.1130/0091-7613(1997)025<0699:ACTOAT>2.3.CO;2.

Sangiorgi, F., H.-J. Brumsack, D. A. Willard, S. Schouten, C. Stickley, M. O'Regan, G.-J. Reichart, J. S. Sinninghe Damsté, and H. Brinkhuis (2008), A 26 million year gap in the central Arctic record at the greenhouse–icehouse transition: Looking for clues, *Paleoceanography*, *23*, PA1S04, doi:10.1029/2007PA001477.

Shipley, T. H., M. K. Houston, R. T. Buffler, F. J. Shaub, K. J. McMillan, J. W. Ladd, and J. L. Worzel (1979), Seismic reflection evidence for the widespread occurrence of possible gas hydrate horizons on continental slopes and rises, *AAPG Bull.*, *63*, 2201–2213.

Sloan, E. D. (1998), Clathrate Hydrates of Natural Gases, 2nd ed., Marcel Dekker, New York.

Sorokin, M. Y., Y. Y. Zamansky, A. E. Langinen, H. R. Jackson, and R. Macnab (1999), Crustal structure of the Makarov Basin, Arctic Ocean determined by seismic refraction, *Earth Planet. Sci. Lett.*, *168*, 187–199, doi:10.1016/S0012-821X(99)00049-7.

St. John, K. (2008), Cenozoic ice-rafting history of the central Arctic Ocean: Terrigenous sands on the Lomonosov Ridge, *Paleoceanography*, *23*, PA1S05, doi:10.1029/2007PA001483.

Stein, R., R. Usbeck, and K. Polozek (1999), Continous whole-core logging of wet bulk density, P wave velocity and magnetic susceptibility, in *ARCTIC 98: The Expedition ARK-XIV/1a of RV Polarstern in 1998*, edited by W. Jokat, *Ber. Polarforsch.*, *308*, 49–57, doi:10013/epic.10311.d001.

Sweeney, J. F., J. R. Weber, and S. M. Blasco (1982), Continental ridges in the Arctic Ocean: LOREX constraints, *Tectonophysics*, *89*, 217–237, doi:10.1016/0040-1951(82)90039-7.

Taylor, P. T., L. C. Kovacs, P. R. Vogt, and G. L. Johnson (1981), Detailed aeromagnetic investigation of the Arctic Basin, 2, *J. Geophys. Res.*, *86*, 6323–6333.

Trehu, A. M., C. Ruppel, M. Holland, G. R. Dickens, M. E. Torres, T. S. Collett, D. Goldberg, M. Riedel, and P. Schultheiss (2006), Gas hydrates in marine sediments, lessons from scientific ocean drilling, *Oceanography*, *19*(4), 124–142.

Vanneste, M., S. Guidard, and J. Mienert (2005), Bottom-simulating reflections and geothermal gradients across the western Svalbard margin, *Terra Nova*, *17*, 510–516, doi:10.1111/j.1365-3121.2005.00643.x.

Vogt, P. R., P. T. Taylor, L. C. Kovacs, and G. L. Johnson (1979), Detailed Aeromagnetic investigation of the Arctic Basin, *J. Geophys. Res.*, *84*, 1071–1089, doi:10.1029/JB084iB03p01071.

Weaver, J. S., and J. M. Stewart (1982), In situ hydrates under the Beaufort Sea shelf, in *Proceedings, Fourth Canadian Permafrost Conference*, edited by H. M. French, pp. 312– 319, Natl. Res. Counc. of Can., Ottawa, Ont.

Weber, J. R., and J. F. Sweeney (1990), Ridges and Basins in the Central Arctic Ocean, in *The Geology of North America,* vol. L, *The Arctic Ocean Region*, edited by A. Grantz, G. L. Johnson, and J. F. Sweeney, pp. 305–36, Geol. Soc. Am., Boulder, Colo.

Wood, W. T., and C. Ruppel (2000), Seismic and thermal investigations of the Blake Ridge gas hydrate area: A synthesis, *Proc. Ocean Drill. Program Sci. Results*, *164*, 253–264.

Xu, W., and C. Ruppel (1999), Predicting the occurrence, distribution and evolution of methane gas hydrate in porous marine sediments, *J. Geophys. Res.*, *104*, 5081–5095, doi:10.1029/1998JB900092.

Yamano, M., S. Uyeda, Y. Aoki, and T. H. Shipley (1982), Estimates of heat flow derived from gas hydrates, *Geology*, *10*, 339–342, doi:10.1130/0091-7613(1982)10<339:EOHFDF>2.0.CO;2.

K. Moran and M. O'Regan, Graduate School of Oceanography, University of Rhode Island, Narragansett, RI 02882, USA.